Proceedings of the 50th International School & Conference on the Physics of Semiconductors

Surface Plasmon Interference Device as a Source of Near-Field Power for Photoluminescence

M. Kvapil[a,b], T. Šikola[a,b] and V. Křápek[a,b,*]

[a] *Institute of Physical Engineering, Brno University of Technology, Technická 2, 616 69 Brno, Czech Republic*
[b] *Central European Institute of Technology, Brno University of Technology, Purkyňova 123, 612 00 Brno, Czech Republic*

Doi: 10.12693/APhysPolA.142.668 *e-mail: krapek@vutbr.cz

We theoretically demonstrate that a simple device consisting of an opaque gold layer with subwavelength slits — the so-called surface plasmon interference device — is capable of transforming the far-field optical power to the near-field one. Optimized slits yield a high conversion efficiency amounting to 45% in terms of the near-field to far-field electric intensity ratio. With a single linear slit arrangement, a propagating wave with a homogeneous field distribution is formed, attributed to surface plasmon polaritons based on its polarization properties. On the other hand, with the slit arrangement supporting interference, it is possible to obtain a standing wave with characteristic spatially modulated interference fringes and spatially separate polarization components. A circular slit can be used for focusing the near-field, with the possibility of obtaining a considerably enhanced field with respect to the excitation. We discuss the implication of the enhanced near-field for the near-field excitation of photoluminescence with the capability to bring a spatial resolution of the photoluminescence spectroscopy beyond the diffraction limit.

topics: surface plasmon polariton, near field, photoluminescence

1. Introduction

Photoluminescence spectroscopy is an excellent diagnostic tool for monitoring electronic transitions in various physical systems. It offers a very good spectral resolution down to units or tens of μeV, allowing one to monitor, e.g., fine structure splitting in quantum dots [1]. A temporal resolution allows monitoring of most electronic transitions including several ps dynamics of transition metal dichalcogenides [2]. Photoluminescence spectroscopy is also non-destructive, exerts a negligible influence on the studied system, imposes no limitations on the studied specimen, and offers excellent sensitivity down to individual photons due to spectral decoupling of the response from the excitation [3]. However, the spatial resolution of the photoluminescence spectroscopy is only mediocre, restricted by the diffraction limit to roughly half a wavelength of light (several hundreds of nanometers). First, this is much worse than the spatial resolution offered by both electron microscopy [4] and scanning probe microscopy. Second, such spatial resolution is insufficient to study contemporary nanostructures and nanomaterials, including, e.g., quantum dots [5], metasurfaces [6], or individual parts of a transistor.

Fortunately, the diffraction limit is only a practical restriction, not a fundamental limit. Even its existence in the far-field has been recently questioned with the discovery of superoscillations [7]. The near-field systems then offer numerous approaches to overcome the diffraction limit and focus the electromagnetic field to subwavelength (and, in some cases, indeed deeply subwavelength) spots. The light focusing beyond the diffraction limit has been demonstrated, e.g., with surface plasmon polaritons (SPP), localized surface plasmons [8], or hyperbolic meta-materials. For photoluminescence spectroscopy with a high spatial resolution, it is vital to excite and collect the luminescence in the near-field.

One of the possible near-field sources is represented by a so-called surface plasmon interference device (SPID). The SPID consists of an opaque metallic layer with subwavelength slits acting as sources of SPP. SPIDs have been utilized to study the properties of SPP, including their wavelength, phase, ultrafast dynamics, or ability to form vortex structures [9–11]. In this contribution, we theoretically examine the possibility of employing SPID as a near-field excitation source for luminescence. We evaluate and optimize the far-field to near-field

conversion efficiency, demonstrate a truly near-field character of the converted light, and discuss its polarization properties.

2. Theory

All simulations utilize a finite difference in time domain (FDTD) approach implemented within a photonic simulation tool Ansys Lumerical. The simulation area has been discretized with a grid step of 5 nm for 2D simulations and 10 nm for 3D simulations. All simulations comprised three materials: semiinfinite silicon dioxide substrate, gold, and air. Their dielectric functions were, respectively, taken from [12], taken from [13], set to 1. The results are presented for the excitation wavelength of 633 nm, where the dielectric function of gold reads $\varepsilon_{\mathrm{Au}} = -10.8755 + 0.844765\mathrm{i}$.

A typical simulation consisted of a plane wave source positioned at the bottom of the simulated area, a gold layer with subwavelength slits, and monitors recording the distribution of the electromagnetic field. In the optimization of slit properties, the thickness of the gold layer is varied in the range of 100–750 nm, and the width of the slit is varied in the range of 50–550 nm. For the other simulations, optimized properties of the slit exhibiting maximum transmission are used, i.e., the width of 310 nm and the length (corresponding to the thickness of gold) of 360 nm.

3. Results

3.1. Surface plasmon polariton

To understand and interpret the formation of the near-field on a SPID, it is worth revisiting the properties of a surface plasmon polariton on a planar air–gold interface. In our study, we will focus on a specific photon energy of 1.96 eV (corresponding to the wavelength of 633 nm). Naturally, the value is inspired by the emission wavelength of traditional He–Ne lasers, which has translated into modern semiconductor-based substitutes. At the same time, it is the high-energy limit for gold plasmonic structures, whose properties deteriorate above 2 eV due to the onset of interband transitions. Finally, such photon energy is sufficient for the excitation of photoluminescence of many important materials and structures, such as silicon nanocrystals, GaAs quantum dots, or transition metal dichalcogenides.

The derivation of the SPP properties can be found in standard textbooks [14]. The propagation wave number of SPP reads

$$\beta = k_0 \sqrt{\frac{\varepsilon_{\mathrm{Au}}\varepsilon_{\mathrm{air}}}{\varepsilon_{\mathrm{Au}} + \varepsilon_{\mathrm{air}}}}, \tag{1}$$

where $k_0 = 2\pi/\lambda$ is the free space wave number, and $\varepsilon_{\mathrm{Au}}$ and $\varepsilon_{\mathrm{air}}$ are the dielectric functions of gold and air, respectively. With $\lambda = 633$ nm, $\varepsilon_{\mathrm{Au}} = -10.8755 + 0.844765\mathrm{i}$, and $\varepsilon_{\mathrm{air}} = 1$, we retrieve the SPP wavelength $\lambda_{\mathrm{SPP}} = 2\pi/\mathrm{Re}(\beta) = 603$ nm and its propagation length $L_{\mathrm{SPP}} = 2/\mathrm{Im}(\beta) = 49$ μm. Into the air, the electric field decays with the distance z from the interface as $E = E_0 \exp(k^z_{\mathrm{air}} z)$ with

$$k^z_{\mathrm{medium}} = \sqrt{\beta^2 - \varepsilon_{\mathrm{medium}} K_0^2},$$
$$\mathrm{medium} \in \{\mathrm{air}, \mathrm{Au}\}. \tag{2}$$

The corresponding field confinement length reads $z_{\mathrm{air}} = 2/\mathrm{Re}(k^z) = 634$ nm.

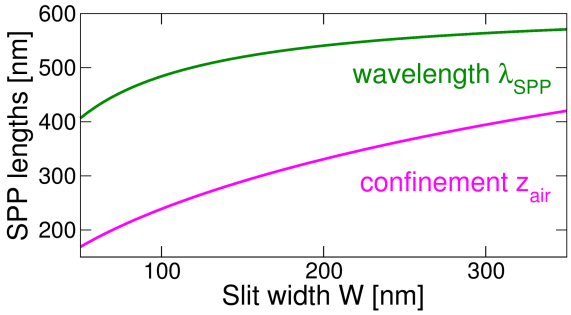

Fig. 1. SPP wavelength λSPP and field confinement length from the side of air z_{air} calculated for a MIM heterostructure representing an infinite linear slit as a function of the slit width W.

For the propagation of SPP through a narrow slit of the width W, a model of metal–insulator–metal (MIM) heterostructure is applicable. Following [14], we found an implicit equation for the propagation wave number β reading

$$\tanh(k^z_{\mathrm{air}} W/2) = -\frac{k^z_{\mathrm{Au}}\varepsilon_{\mathrm{air}}}{k^z_{\mathrm{air}}\varepsilon_{\mathrm{Au}}}. \tag{3}$$

The SPP wavelength and field confinement length obtained by solving this equation are shown in Fig. 1. For narrow slits, the wavelength is considerably smaller than for a planar air–gold interface.

3.2. Optimization of single slit

A conversion of the incident plane wave to the SPP through the subwavelength slits can result in substantial power loss. It is thus important to optimize the properties of the slit for maximum conversion efficiency. A scheme of the optimization simulation is shown in Fig. 2a. The plane wave impinges from the bottom (i.e., from the side of the substrate) onto a gold layer of the thickness L with a slit of the width W. We consider the slit of an infinite breadth (in the direction perpendicular to Fig. 2a). This brings the benefits of a homogeneous field distribution without diffraction effects from the slit of a finite breadth and the possibility of two-dimensional simulation with reduced complexity. Figure 2b shows a field distribution for transmission through the optimized slit ($L = 360$ nm, $W = 310$ nm). We plot the out-of-plane component not present in the incident plane wave. Therefore, only the scattered field is visible. Gold blocks the propagation of the field; it is therefore represented by white color. The field can be classified into

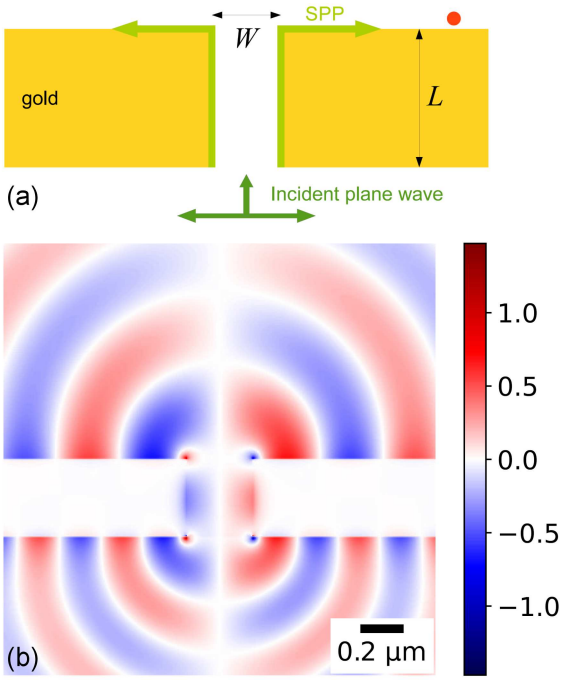

Fig. 2. (a) A scheme of the simulation. A plane wave impinges at the gold layer with a slit from the bottom. SPPs propagate through a slit and at the upper air–gold interface, as indicated by light green arrows. The slit length L and width W are indicated by black arrows. The red point schematically represents a spot 5 μm away from the slit edge where the SPP field is evaluated for the slit optimization. (b) Electric field represented by a real part of the out-of-plane (vertical) component for a transmission through the optimized slit (L = 360 nm, W = 310 nm). White area corresponds to gold.

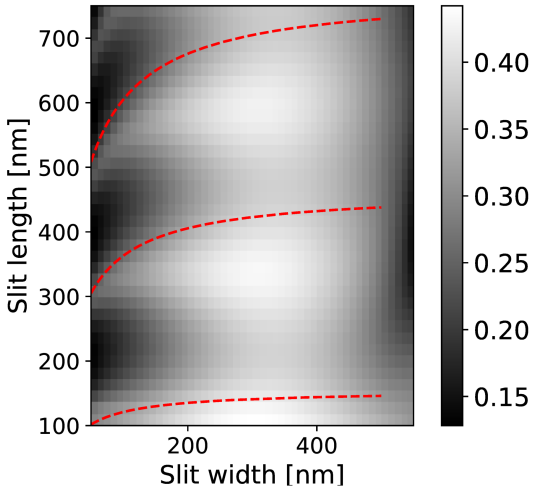

Fig. 3. A magnitude of the electric field recorded at the air–gold interface 5 μm away from the slit edge for a range of slit widths and lengths. Red dashed lines correspond to a constructive interference condition.

three contributions: (i) the slit allows the transmission through the gold layer by means of a surface wave attributed to SPP; (ii) SPPs also propagate along both the upper and lower interface of gold; (iii) the diffraction of the incident plane wave at the bottom edges of the slits and the diffraction of the slit SPP at the top edges of the slit result in reflected and transmitted far-field wave, approximately cylindrical.

To find the optimum parameters of the slit, we set the near-field magnitude at the upper air–gold as the figure of merit. To exclude the possible contribution of the field diffracted at the slit, we monitor the field 20 nm above the upper gold surface at a distance of 5 μm away from the slit. We vary the length and width of the slit in a reasonable range of values. The width is kept under the wavelength to exclude the transmission of the far-field through a slit, while the bottom limit for length is set by the need for the opacity of the gold layer, and the upper limit is set well above the SPP wavelength to observe a full range of the interference effects. The field is found to have a vectorial nature with the ratio of the out-of-plane (OOP) component (perpendicular to the gold surface) to the in-plane (IP) component (parallel to the gold surface) ranging between 3.4 and 3.6. This confirms the attribution of the field to SPP, for which the ratio of the OOP and IP electric intensities read $X = |\beta/k^z| = 3.3$.

The magnitude of the field at the point of interest is shown in Fig. 3. As the slit length is varied, clear interference patterns are observed. The lengths corresponding to bright interference stripes $L^{\max}$ are described rather well by a common constructive interference condition $L^{\max} = m\lambda_{\mathrm{SPP}}/2 + \Delta_R$, which is also displayed in Fig. 3 (red lines). Here, Δ_R represents the phase accumulated at the reflections of the SPP at the ends of the slit, and by fitting to the maxima it is determined as $\Delta_R \approx \lambda_{\mathrm{SPP}}/4$. The slit width influences the field magnitude mostly indirectly by affecting the wavelength of interfering SPP, with the effect being most prominent for the widths below 100 nm. There is also some additional effect manifested by a brightening for slit widths around 300 nm, probably related to the bending efficiency of SPP from the slit to the upper gold surface. The optimum slit length and width corresponding to the largest field are 360 nm and 310 nm, respectively. The optimized slits will be utilized to design realistic surface plasmon interference devices that will be discussed in the following section.

3.3. Colinear and circular surface plasmon interference device

We will now focus on two important arrangements of SPID and their fields. They are both formed by a gold layer with a thickness of 360 nm (corresponding to the slit length) with a slit width of 310 nm. For both, we utilized the same excitation by a plane wave with a wavelength of 633 nm and a linear polarization along the horizontal axis of

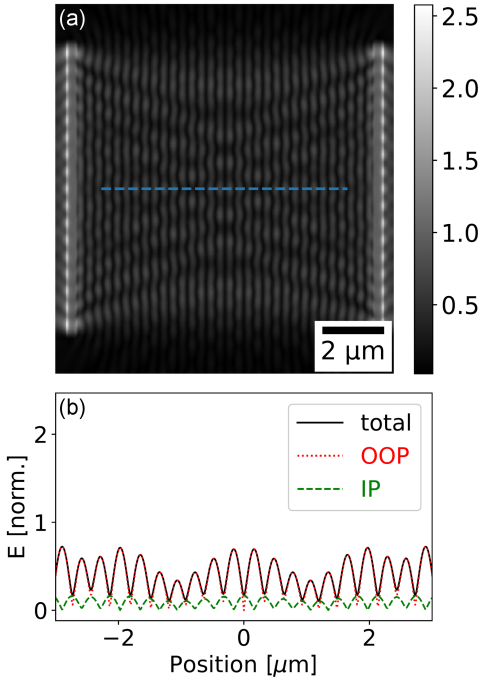

Fig. 4. Colinear SPID: (a) Magnitude of the total electric field at the height of 20 nm above the air–gold interface. (b) Magnitudes of the total (black), OOP (red), and IP (green) electric field along the blue dashed line (parallel with the polarization of the incident plane wave) shown in panel a. All field magnitudes are normalized to the electric field of the incident plane wave.

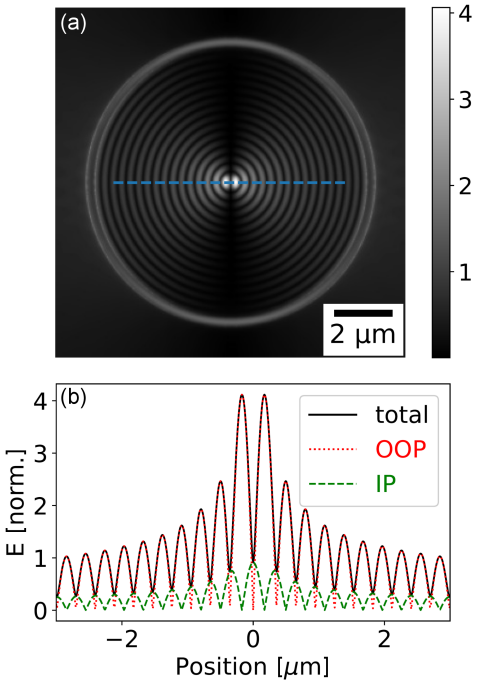

Fig. 5. Circular SPID: (a) Magnitude of the total electric field at the height of 20 nm above the air–gold interface. (b) Magnitudes of the total (black), OOP (red), and IP (green) electric field along the blue dashed line (parallel with the polarization of the incident plane wave) shown in panel a. All field magnitudes are normalized to the electric field of the incident plane wave.

Figs. 4a and 5a. The first arrangement, a colinear SPID, is composed of two parallel slits positioned at opposite sides of a square with a side length of 10 μm, i.e., the slits are 10 μm broad and 10 μm apart from each other. The second arrangement, a circular SPID, is composed of a single circular slit with a diameter of 10 μm.

Figure 4 shows the field formed at the colinear SPID. We observe interference stripes corresponding to the interference of two counterpropagating plane waves, with the intensity modulated by the diffraction at the slits of finite breadth (we reserve the term length of the slit for the thickness of the gold layer). The phase shift between the OOP and IP components of SPP translates into the spatial separation of the interference fringes for both components. This unusual polarization characteristic allows, for example, to perform polarization-resolved measurements on a single SPID only by changing the position of the detector. From the linear cross-sections of the field distribution, we can estimate the SPP wavelength by counting the bright stripes at a certain range of coordinates. We find the distance between the first and last of 20 central bright stripes, corresponding to $9.5\lambda_{\mathrm{SPP}}$, to be 5.813 μm, yielding $\lambda_{\mathrm{SPP}} = 612$ nm. This is not so far from the expected value of 603 nm, with the discrepancy assigned to the diffraction effects. Disregarding the interference and diffraction effects, the magnitude of the field is distributed rather homogeneously over the whole SPID, and at the brightest spots, it reaches about 70% of the incident electric field magnitude.

A striking feature of the circular SPID, the field of which is shown in Fig. 5, is the concentration and enhancement of the field at the center of SPID, where the OOP component is enhanced four times with respect to the excitation and even the weaker IP component reaches 80% of the excitation intensity. Further, the intensity distribution is inhomogeneous, with bright spots concentrated in the bowtie area parallel to the polarization. The orientation of the bowtie can be controlled by incident polarization. In this way, we can excite different areas within the SPID. Finally, the high symmetry of the circular SPID results in circular interference fringes unperturbed by the diffraction.

4. Conclusions

We have demonstrated that SPID is capable of converting the far-field of the incident plane wave to the near-field of SPP propagating along the SPID. The near-field character of the transmitted wave is corroborated by its polarization properties (in-plane

to out-of-plane intensity ratio) and its wavelength, both of which correspond very well to SPP on the air–gold interface of the SPID. The conversion efficiency for one extended linear slit reaches up to 45% in terms of the electric near-field magnitude related to the incident electric far-field magnitude. Similar magnitudes are obtained for a SPID formed by two colinear slits. By judiciously designed slit, it is possible to achieve focusing and enhancement directly in the near-field — a SPID with a circular slit exhibits enhancement of the incident field by a factor of 4. The standing waves formed by SPIDs also exhibit a spatial separation of two polarization components of the electric field. With all these properties, SPIDs represent efficient sources of near-field electromagnetic power that can be used as an excitation source for luminescence with subwavelength spatial resolution, high intensity, and non-trivial polarization properties.

Acknowledgments

This work was supported by Czech Science Foundation, grant No. 19-06621S.

References

[1] Y.H. Huo, V. Křápek, A. Rastelli, O.G. Schmidt, *Phys. Rev. B* **90**, 041304 (2014).

[2] D. Lagarde, L. Bouet, X. Marie, C.R. Zhu, B.L. Liu, T. Amand, P.H. Tan, B. Urbaszek, *Phys. Rev. Lett.* **112**, 047401 (2014).

[3] I. Aharonovich, D. Englund, M. Toth, *Nat. Photon.* **10**, 631 (2016).

[4] F.J. García de Abajo, *Rev. Mod. Phys.* **82**, 209 (2010).

[5] L. Wang, V. Křápek, F. Ding, F. Horton, A. Schliwa, D. Bimberg, A. Rastelli, O.G. Schmidt, *Phys. Rev. B* **80**, 085309 (2009).

[6] N. Yu, F. Capasso, *Nat. Mater.* **13**, 139 (2014).

[7] F.M. Huang, N. Zheludev, Y. Chen, F.J. Garcia de Abajo, *Appl. Phys. Lett.* **90**, 091119 (2007).

[8] F. Benz, M.K. Schmidt, A. Dreismann, R. Chikkaraddy, Y. Zhang, A. Demetriadou, C. Carnegie, H. Ohadi, B. de Nijs, R. Esteban, J. Aizpurua, J.J. Baumberg, *Science* **354**, 726 (2016).

[9] P. Dvořák, Z. Édes, M. Kvapil, T. Šamořil, F. Ligmajer, M. Hrtoň, R. Kalousek, V. Křápek, P. Dub, J. Spousta, P. Varga, T. Šikola, *Opt. Express* **25**, 16560 (2017).

[10] P. Dvořák, M. Kvapil, P. Bouchal, Z. Édes, T. Šamořil, M. Hrtoň, F. Ligmajer, V. Křápek, T. Šikola, *Nanoscale* **10**, 21363 (2018).

[11] G. Spektor, D. Kilbane, A.K. Mahro, B. Frank, S. Ristok, L. Gal, P. Kahl, D. Podbiel, S. Mathias, H. Giessen, F.-J.M. zu Heringdorf, M. Orenstein, M. Aeschlimann, *Science* **355**, 1187 (2017).

[12] E.D. Palik, E.J. Prucha, *Handbook of Optical Constants of Solids*, Academic Press, Boston (MA) 1997.

[13] M. Weber, *Handbook of Optical Materials*, 1st ed., CRC Press, 2002.

[14] S. Maier, *Plasmonics: Fundamentals and Applications* Springer, 2007.